Wetting of water on hexagonal boron nitride@Rh(111): a QM/MM model based on atomic charges derived for nano-structured substrates

Golze, Dorothea ; Hutter, Jürg ; Iannuzzi, Marcella

Abstract: The wetting of water on corrugated and flat hexagonal boron nitride (h-BN) monolayers on Rh(111) is studied within a hybrid quantum mechanics/molecular mechanics (QM/MM) approach. Water is treated by QM methods, whereas the interactions between liquid and substrate are described at the MM level. The electrostatic properties of the substrate are reproduced by assigning specifically generated partial charges to each MM atom. We propose a method to determine restrained electrostatic potential (RESP) charges that can be applied to periodic systems. Our approach is based on the Gaussian and plane waves algorithm and allows an easy tuning of charges for nano-structured substrates. We have successfully applied it to reproduce the electrostatic potential of the corrugated and flat h-BN/Rh(111) known as nanomesh. Molecular dynamics simulations of water films in contact with these substrates are performed and structural and dynamic properties of the interfaces are analyzed. Based on this analysis and on the interaction energies between water film and substrate, we found that the corrugated nanomesh is slightly more hydrophilic. On a macroscopic scale, we expect a smaller contact angle for a droplet on the corrugated surface.

DOI: https://doi.org/10.1039/c4cp04638b

Wetting of water on hexagonal boron nitride@Rh(111): A QM/MM model based on RESP charges derived for nano-structured substrates†

Dorothea Golze,* Jürg Hutter, and Marcella Iannuzzi

Received Xth XXXXXXXXXX 20XX, Accepted Xth XXXXXXXXX 20XX
First published on the web Xth XXXXXXXXXX 200X
DOI: 10.1039/b000000x

The wetting of water on corrugated and flat hexagonal boron nitride (*h*-BN) monolayers on Rh(111) is studied within a hybrid quantum mechanics/molecular mechanics (QM/MM) approach. Water is treated by QM methods, whereas the interactions between liquid and substrate are described at the MM level. The electrostatic properties of the substrate are reproduced by assigning specifically generated partial charges to each MM atom. We propose a method to determine restrained electrostatic potential (RESP) charges that can be applied to periodic systems. Our approach is based on the Gaussian and plane waves algorithm and allows an easy tuning of charges for nano-structured substrates. We have successfully applied it to reproduce the ESP of the corrugated and flat (*h*-BN)/Rh(111) known as nanomesh. Molecular dynamics simulations of water films in contact with these substrates are performed and structural and dynamic properties of the interfaces are analyzed. Based on these analyses and on the interaction energies between water film and substrate, we found that the corrugated nanomesh is slightly more hydrophilic. On a macroscopic scale, we predict a smaller contact angle for a droplet on the corrugated surface.

1 Introduction

Wetting behavior of liquid water on surfaces is a long-standing research field with major importance for technological applications such as sensors and coatings.[1,2] Deeper understanding of the wetting at functional surfaces is especially important for fluids confined in nanoscale structure. Controlling the wettability at the nanoscale potentially enables the development of smart surfaces and nano-based devices. In this respect, versatile templates like single layers of hexagonal boron nitride (*h* -BN) on metal surfaces are of particular interest. Monolayers of *h*-BN have been epitaxially grown on hot metallic surfaces by chemical vapor decomposition of borazine[3] molecules. The structural and electronic properties of BN can be tuned by the choice of the metal.[4,5] *h*-BN structures have been prepared on a range of transitions metals, such as Rh(111),[3,6] Ni(111),[7–9] Cu(111),[7,10] Ir(111)[11,12] and several others.[13–17]

On Rh(111), a corrugated superstructure is formed with a periodicity of 3.2 nm induced by the lattice mismatch between BN and Rh.[6,18,19] The unit cell of this so-called nanomesh is given by 13×13 BN units on 12×12 Rh(111). The nanomesh is characterized by a regular arrangement of 2 nm "pores" separated by regions less tightly bound to Rh(111) called "wire". The corrugation causes a modulation in the electrostatic potential (ESP) above the BN layer, which is thought to be responsible for trapping molecules in the pores.[20] Preferential adsorption in the pore regions has been studied for organic molecules,[6,21–23] noble gas atoms[24] and to great extend for small water clusters.[25–29] The mesh structure is very robust, stable in gas phase,[30] survives immersion in liquids[6,31] and withstands temperature up to 1000 K.[32] By intercalation of atomic H, which strongly binds to the Rh surface, the interaction between nitrogen and Rh is weakened and the *h*-BN layer becomes much flatter. However, this modification can be easily reversed by desorption of hydrogen, thus recovering the original nanomesh. By reversible intercalaction and removal of H atoms, switching between corrugated and flat structure is then possible. Since the corrugation determines the functionality of the surface, the interactions between molecules and substrate can be reversibly altered. This is also interesting in the context of wetting in order to control the hydrophilicity of the surface.

In this work, the wetting of liquid water on the corrugated and the H-intercalated nanomesh are studied. The two substrates are in the following referred to as nm and nm-H, respectively. A full quantum mechanical description of the wetting by density functional theory (DFT) is not affordable because of computational limitations. Instead, a computationally less expensive hybrid scheme combining quantum mechanics (QM) with molecular mechanics (MM) is used.[33] In our QM/MM setup, the liquid water is described by DFT, whereas the substrate and the interactions between substrate and molecules are treated at the MM level of theory. A similar setup has been used in our previous work and proved to

† Electronic Supplementary Information (ESI) available: [Table S1 and Figures S1-S5]. See DOI: 10.1039/b000000x/

Address, Department of Chemistry, University of Zürich, Winterthurerstrasse 190, CH-8057 Zürich, Switzerland. E-mail: dorothea.golze@chem.uzh.ch

be successful for adsorbate-metal systems.[34] In order to properly describe the electrostatic interactions between substrate and liquid, the very specific modulated features of the ESP above the nanomesh have to be reproduced. These features have been extensively characterized by DFT calculation of the electronic structure of the nanomesh.[5,28] MM force fields typically rely on partial atomic charges to model electrostatic interactions. A popular approach is to apply a fitting procedure in order to determine the charges that optimally reproduce a given ESP. Often, restraints and constraints are also implemented to guarantee physically meaningful values of the resulting charges, which are then called RESP charges.[35] This approach is widely used for nonperiodic molecular systems. Fitting RESP charges for periodic systems leads to additional difficulties due to the long-range nature of the ESP. Periodic RESP schemes were derived and successfully applied to molecular crystalline systems like metal organic frameworks.[36,37] We present in this work a novel adaptation and extension of the RESP charge fitting procedure for periodic systems, like slab systems. Our approach is based on a mixed Gaussian and plane wave (GPW) formalism and hence naturally dealing with periodic ESPs and additionally circumventing problems related to the their ill-defined reference state.

In the next section, the theory and implementation of our periodic RESP model are described. Adjustable parameters of the QM/MM setup are discussed and validated. RESP charges are derived for nm and nm-H and the accuracy of the fitted potential is assessed. Molecular dynamics (MD) simulations of liquid water at nm and nm-H interfaces are performed using the previously described QM/MM setup. Structural and dynamic properties are discussed for insight in the wetting at molecular scale. We address interactions energies and the contact angle of a water droplet on these substrates to evaluate and compare the hydrophilicity in macroscopic terms.

2 Periodic RESP fitting

2.1 Theory and implementation

For obtaining RESP charges, a quantum chemical calculation is performed to generate a reference ESP V_{QM}. A set of atomic point charges $\{q_a\}$ is derived such that the difference between V_{QM} and the potential V_{RESP} generated by $\{q_a\}$ is minimized. This minimization is performed in a least squares fitting procedure at defined grid points $\mathbf{r}_k$. The residual that needs to be minimized is given by

$$R_{\mathrm{esp}} = \frac{1}{N}\sum_{k}^{N}(V_{\mathrm{QM}}(\mathbf{r}_k) - V_{\mathrm{RESP}}(\mathbf{r}_k))^2, \tag{1}$$

where N is the total number of grid points included in the fitting procedure. The optimal choice of $\{\mathbf{r}_k\}$ depends on the system and is discussed below. In our approach, the point charges are represented as Gaussian functions with fixed width α. The resulting charge distribution ρ is defined as

$$\begin{aligned}\rho(\mathbf{r}) &= \sum_a q_a g_a(\mathbf{r},\mathbf{R}_a) \\ &= \sum_a q_a \left(\frac{\alpha}{\pi}\right)^{\frac{3}{2}} exp(-\alpha|\mathbf{r}-\mathbf{R}_a|^2),\end{aligned} \tag{2}$$

where $\mathbf{R}_a$ is the position of atom a and g_a is the normalized spherical Gaussian function centered at a. The potential V_{RESP} generated by ρ and given by

$$V_{\mathrm{RESP}}(\mathbf{r}) = \int \frac{\rho(\mathbf{r}')}{|\mathbf{r}'-\mathbf{r}|}\mathrm{d}\mathbf{r}' = \sum_a q_a \int \frac{g_a(\mathbf{r}',\mathbf{R}_a)}{|\mathbf{r}'-\mathbf{r}|}\mathrm{d}\mathbf{r}' \tag{3}$$

is inserted in eq 1. To avoid physically meaningless atomic charges, restraints and constraints are introduced in the fitting procedure. The total residual is then

$$R = R_{\mathrm{esp}} + R_{\mathrm{rest}} + R_{\mathrm{const}}. \tag{4}$$

To address restraints, a harmonic penalty function is chosen,

$$R_{\mathrm{rest}} = \beta\sum_j (q_j - t_j)^2, \tag{5}$$

where t_j is the target charge and β a scaling factor determining the strength of the restraint. Various constraints can be employed. Usually, the sum of all fitted charges is constrained to the total charge of the system, see ref[36] for details.

When calculating RESP charges for periodic systems, periodic boundary conditions (PBC) have to be employed for the calculation of V_{RESP} . Our approach is part of the CP2K program package[38,39] and based on the GPW formalism. Within the GPW approach, the RESP charge distribution ρ can be represented on a regular grid. Fast Fourier transforms (FFT) are used to change the representation from real space $\rho(\mathbf{r})$ to reciprocal space $\rho(\mathbf{G})$, where $\mathbf{G}$ is the reciprocal lattice vector. Since the Poisson equation is solved in reciprocal space, the obtained potential $V_{\mathrm{RESP}}(\mathbf{G})$ is naturally periodic. An inverse FFT is used to transfer the potential back to real space.

Minimizing eq 4 with respect to the unknowns $\{q_a\}$ yields a linear set of equations,

$$\frac{\partial R}{\partial q_a} = -C_a + \sum_b q_b T_{ab} + 2\beta(q_a - t_a) + \lambda = 0 \tag{6}$$

where λ is the Lagrange multiplier associated with a constraint on the total charge. The vector $\mathbf{C}$ is given by

$$C_a = \frac{2}{N}\sum_k V_{\mathrm{QM}}(\mathbf{r}_k)v_a(\mathbf{r}_k) \tag{7}$$

and matrix $\mathbf{T}$ by

$$T_{ab} = \frac{2}{N}\sum_b\sum_k q_b v_a(\mathbf{r}_k)v_b(\mathbf{r}_k). \tag{8}$$

Loop over all a atoms

Collocate $g_a(\mathbf{r})$ on the real space grid

Transfer to reciprocal space: $g_a(\mathbf{r}) \xrightarrow{\text{FFT}} g_a(\mathbf{G})$

Solve Poisson equation: $g_a(\mathbf{G}) \longrightarrow v_a(\mathbf{G})$

Transfer back to real space: $v_a(\mathbf{G}) \xrightarrow{\text{FFT}^{-1}} v_a(\mathbf{r})$

Loop over all atoms b

T: Calculate product $v_a(\mathbf{r}_k)v_b(\mathbf{r}_k)$ at grid points $\mathbf{r}_k$

End b loop

C: Calculate product $V_{\text{QM}}(\mathbf{r}_k)v_a(\mathbf{r}_k)$ at grid points $\mathbf{r}_k$

End a loop

Fig. 1 Pseudocode for calculating matrix **T** and vector **C**.

The potential $v_a(\mathbf{r}_k)$ is generated by one single Gaussian charge at atom a and given by

$$v_a(\mathbf{r}_k) = \int \frac{g_a(\mathbf{r}', \mathbf{R}_a)}{|\mathbf{r}' - \mathbf{r}|} \mathrm{d}\mathbf{r}'. \tag{9}$$

The procedure to obtain periodic solutions for $v_a(\mathbf{r}_k)$ and subsequently T_{ab} and C_a is shown in Figure 1. The potential $v_a(\mathbf{r}_k)$ is transferred to real space by an inverse FFT step once the Poisson equation has been solved in reciprocal space. The matrix and vector elements are then computed on the real space grid for the set of pre-defined grid points $\{\mathbf{r}_k\}$.

Our implementation of periodic RESP fitting utilizes the massive parallelization procedures already present in CP2K and enables an efficient computation of RESP charges also for large systems.

In calculations of periodic ESP, care must be taken of the arbitrariness of the reference state. Campañá et al.[36] pointed out that reference and fitted potential suffer from different constant offsets they addressed by modifying the residual R accordingly. However, in our approach V_{QM} and V_{RESP} are computed in the same way using the GPW scheme. Hence they have the same constant offset which cancels out when evaluating R_{esp}.

2.2 Sampling of fit points

A set of grid points is chosen where the atomic charges are fitted to correctly reproduce the reference potential. In molecular calculations, the grid points that are included in the fitting are usually chosen to lie outside the Van der Waals region where intermolecular interactions have to be described correctly. In addition, region of high electron density, e.g., within the Van der Waals region, cannot be modeled accurately by atomic charges anyway. For slab-like systems, the ESP has to be accurately reproduced over the surface which is especially important when studying adsorption processes. A good choice is to sample the ESP in a specified range of, e.g., 2-4 Å above the surface. In case of corrugated substrates like nm, our sampling is flexible enough to follow the corrugation in a defined volume above the BN layer as displayed in Figure 2.

3 Computational Details

3.1 Charge fitting

The superstructure of nm is represented by a hexagonal arrangement of 13×13 h-BN on 12×12 replica of the Rh unit cell. For nm-H, 12×12 H atoms are intercalated between the h-BN and the topmost Rh(111) layer. We model nm by a slab of seven Rh layers terminated on both sides by one h-BN monolayer. PBC are applied in all calculations. Spurious interactions with periodic images are avoided by adding a vacuum of at least 15 Å in the direction perpendicular to the surface.

All calculations are carried out with the CP2K program package.[38,39] Structure optimization and calculation of V_{QM} for nm and nm-H are performed at the Kohn-Sham DFT level within the GPW approach.[40,41] Single-ζ valence plus polarization (SZVP) basis sets are used to describe the valence electrons of Rh, whereas basis sets of at least double-ζ quality (DZVP) are used for the other elements.[42] Norm-conserving pseudo-potentials[43–45] are employed to approximate the interactions between valence electrons and atomic cores. The exchange and correlation potential is given by the revised Perdew-Burke-Ernzerhof (revPBE)[46] functional. The latter is used in combination with Grimme's D3 correction[47] to account for long-range dispersion interactions. The cutoff for the PW expansion of the auxiliary density is set to 500 Ry. Fermi-Dirac smearing at an electronic temperature of 300 K and Broyden density mixing[48] are employed to guarantee a smooth convergence.

For the fitting procedure of the RESP charges, the total charge of the system is constrained to zero and atoms of pre-defined groups are constrained to carry identical charges. Moreover, restraints are employed as described below. To evaluate the quality of the fit, V_{RESP} is compared to the reference DFT potential by means of the root-mean square (RMS)

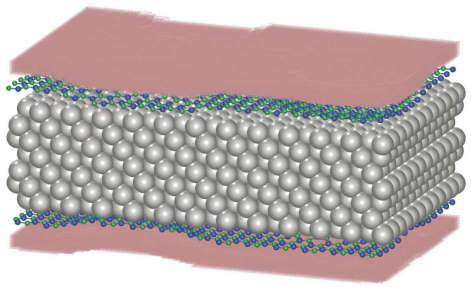

Fig. 2 Grid points sampled in a volume of 2-4 Å above the surface for the symmetric corrugated h-BN/Rh(111) slab. Color code: B green, N blue , Rh gray, grid points pink.

error,

$$\mathrm{RMS} = \sqrt{\frac{\sum_k^N \left(V_{\mathrm{QM}}(\mathbf{r}_k) - V_{\mathrm{RESP}}(\mathbf{r}_k)\right)^2}{N}} \tag{10}$$

and relative root-mean square (RRMS) error

$$\mathrm{RRMS} = \sqrt{\frac{\sum_k \left(V_{\mathrm{QM}}(\mathbf{r}_k) - V_{\mathrm{RESP}}(\mathbf{r}_k)\right)^2}{\sum_k V_{\mathrm{QM}}(\mathbf{r}_k)^2}}. \tag{11}$$

3.2 MD simulations

QM/MM has been used to perform an MD simulation of liquid water at the nm and nm-H interface. For the MD simulations, the hexagonal *h*-BN/Rh(111) slabs have been extended to orthorhombic slabs with 13×26 *h*-BN and 12×24 Rh. Both slabs are surmounted with a 15Å thick water layer consisting of 833 water molecules. A vacuum space of 25 Å is added to prevent interactions with periodic images along the [111] direction. The water layer is treated at the DFT level of theory, whereas the interactions between water and the nanomesh are computed at the MM level. The positions of the substrate atoms are kept fixed in their DFT optimized structure. For the QM part DZVP basis sets, the PBE functional[49] and a PW cutoff of 300 Ry are used.

The electrostatic interactions between water layer and nanomesh are modeled by the RESP charges given in Table 1. The electrostatic coupling procedures implemented in the QM/MM[50,51] part of CP2K are employed to correctly treat the electrostatics with PBC. Note that QM and MM box have been set to the same size in order to avoid computationally expensive decoupling between QM images. To reproduce dispersion and Pauli repulsion between water and nanomesh, an empirical potential of the Lennard Jones (LJ) type is used. The B-O and N-O interaction parameters are $\sigma_{\text{B-O}} = 3.31$ Å, $\sigma_{\text{N-O}} = 3.26$ Å, $\varepsilon_{\text{B-O}} = 0.52$ kJ/mol and $\varepsilon_{\text{N-O}} = 0.63$ kJ/mol. The latter were derived from the B-B and N-N interactions parameter given in ref[52,53] and the O-O parameters of the SCP/Fw water model.[54]

All MD simulations are performed within the canonical (NVT) ensemble using a time step of 0.5 fs. Before starting the actual simulations, all systems have been pre-equilibrated solely by MM for at least 1 ns using the SCP/Fw water potential and temperature annealing up to 300 K. The QM/MM simulations are run at a temperature of 330 K and equilibrated for at least 10 ps. The last 20 ps of the simulation have been used for analysis.

To obtain interaction energies and properties related to the contact angle, a DFT-based MD simulation of a pure 15 Å-thick water slab is performed with the same number of molecules. The interaction energies E_{int} between nm and water film are computed according to

$$E_{\mathrm{int}} = \frac{E_{\mathrm{nm+H_2O}} - (E_{\mathrm{nm}} + E^{\mathrm{slab}}_{\mathrm{H_2O}})}{n_{\mathrm{slab}}}, \tag{12}$$

where $E_{\mathrm{nm+H_2O}}$ denotes the averaged potential energy of nm surmounted with the water layer. E_{nm} is the energy of the substrate only and $E^{\mathrm{slab}}_{\mathrm{H_2O}}$ the averaged energy of the pure water slab. The number of water molecules is declared by n_{slab}.

The contact angle θ of a water droplet on a surface can be estimated from interface energies according to Young's formula[55–57],

$$\cos\theta = \frac{\gamma_{\mathrm{SV}} - \gamma_{\mathrm{SL}}}{\gamma_{\mathrm{LV}}}, \tag{13}$$

where γ_{LV}, γ_{SL} and γ_{SV} represent the energies of the liquid-vacuum, solid-liquid and the solid-vacuum interfaces, respectively. For the nanomesh, γ_{SV} is not accessible since the bulk-phase of nm does not exist and hence no reference value for calculating γ_{SV}. However, the difference of $\cos\theta$ between nm and nm-H can be computed assuming that γ_{SV} is identical for both systems. Following the argumentation in ref[58], we estimate γ_{SL} by the interaction energy given in eq 12 per unit area. For the liquid-vacuum interface, γ_{LV} is approximated by

$$\gamma_{\mathrm{LV}} = \frac{E^{\mathrm{slab}}_{\mathrm{H_2O}} - \frac{n_{\mathrm{slab}}}{n_{\mathrm{bulk}}} E^{\mathrm{bulk}}_{\mathrm{H_2O}}}{2A}, \tag{14}$$

where $E^{\mathrm{bulk}}_{\mathrm{H_2O}}$ is the averaged potential energy for bulk water, n_{bulk} is the number of water molecules in the bulk and A the area defined by the horizontal dimensions of the slab. To assess $E^{\mathrm{bulk}}_{\mathrm{H_2O}}$, bulk water is simulated at the DFT level using a cubic box with 128 water molecules.

4 Tests and results

4.1 Parameter validation

The RESP approach relies on restraining charges during the fitting process, see eq 5. Target values for the charges and the strength of the restraint β are parameter to be tuned carefully. The larger β, the less flexible is the fitting leading to larger RRMS errors. We found that values of $\beta > 10^{-4}$ drastically increase the RRMS value, see Supporting Information (SI) Table S1. Therefore, β was always set to 10^{-4} yielding physical charges and an accurately fitted potential. The target values were partly estimated from unrestrained ESP charges and density derived Blöchl charges.[59]

The Gaussian width α determining the width of the charge distribution ρ is another adjustable parameter in our approach, see eq 2. To evaluate the influence of α on the fitted charges q, test runs of a single *h*-BN sheet have been performed. The dependency of the magnitude of q on α is reported in SI, Figure S1. The charges do not depend on the Gaussian width for values of α larger than 3.0 Å^{-2}. However, the fitting procedure becomes unreliable for smaller values. Small values of α model too broad Gaussian functions describing a uniform charge distribution rather than localized charges, which necessarily leads to wrong results.

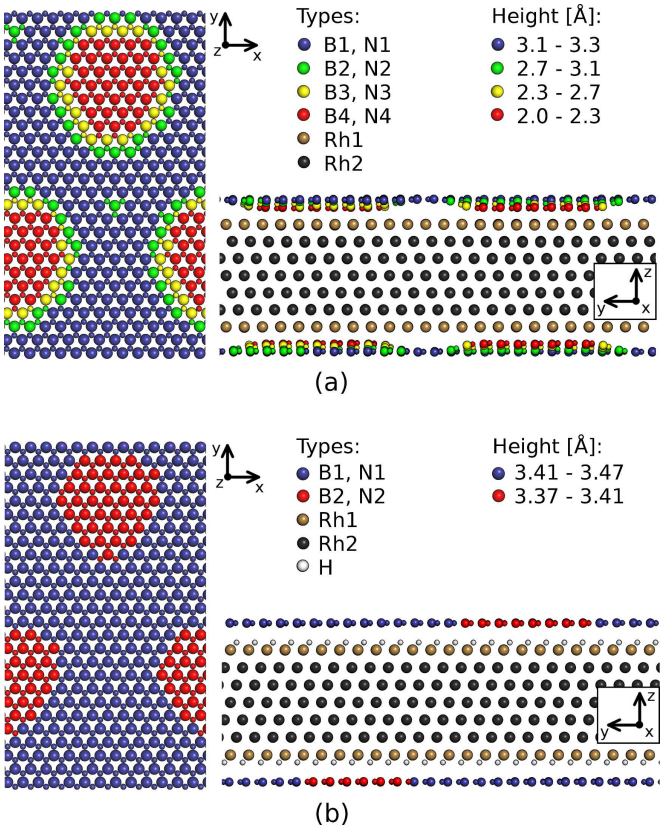

Fig. 3 Assignment of the atom types for (a) nm and (b) nm-H. The height of B and N atoms is measured relative to average height of the topmost Rh layer (Rh1). Top view of the BN layer (left) and side view of the whole symmetric slab (right).

The LJ parameter modeling the dispersion were not specifically optimized for nm and nm-H. To asses the error introduced by inaccurate dispersion interactions, MD simulations of a water slab in contact with a free-standing BN layer have been performed, see Figure S2 (SI). For this system, electrostatic interactions at the interface can be neglected. Comparing the interaction energies obtained by full DFT simulations and QM/MM provides a direct measure of the quality of the LJ parameters given in Section 3.2. The interaction energy based on the LJ parameters is larger by a factor of 1.25 indicating that our QM/MM setup is slightly overestimating the dispersive interactions, see SI.

4.2 Charges fitted for the nanomesh

To reduce complexity, the atoms of the nanomesh have been assigned to different sets. Charges of atoms belonging to the same set are enforced to be identical by constraints. For nm, B and N atoms are divided in four types depending on the height above the topmost Rh layer, see Figure 3. The first set of atoms defines the wire region, the second and third the rim of the pore and the fourth set the pore itself. The same strategy is used for nm-H shown in Figure 3. Since the difference in height between wire and pore is only 0.1 Å for the latter, the atoms are simply assigned to pore and wire establishing no further sets for the transition between the two regions. As shown in Table 1, positive charges are generally obtained for boron and negative charges for nitrogen, which is in agreement with the difference in electronegativity. Comparing the magnitude of charges for B and N atoms, larger values have always been obtained for nitrogen. This is an effect arising from the slightly positive charges of Rh and constraining the total charge to zero. Furthermore, the absolute charge values for B and N are larger in the pore and decrease gradually moving from rim to wire. This is essential to reproduce the modulation of the potential as shown below. The intercalated H atoms for the almost flat nanomesh are negatively charged pointing to a hydride-like character. This seems reasonable because the H monolayer is quasi-bonded to the topmost Rh layer.

RMS and RRMS errors are very small indicating a high quality of the fit. The RRMS errors are smaller[36] or at least comparable[37] to the values reported for the RESP fitting of periodic molecular structures. To gain better insights into the characteristics of the electrostatic potential, the latter is plotted at a height of 4.8 Å above the wire in Figure 4. A strong

Table 1 RESP charges fitted for nm and nm-H. Atom types correspond to the assignment in Figure 3.

nm		nm-H	
atom type	charge	atom type	charge
B1	0.040	B1	0.013
B2	0.048	B2	0.031
B3	0.074	N1	-0.099
B4	0.201	N2	-0.120
N1	-0.139	Rh1	0.000
N2	-0.154	Rh2	0.048
N3	-0.223	H	-0.019
N4	-0.311		
Rh1	0.005		
Rh2	0.046		
RMS	$1.3{\cdot}10^{-5}$	RMS	$5{\cdot}10^{-6}$
RRMS	$2.4{\cdot}10^{-2}$	RRMS	$8{\cdot}10^{-3}$

Table 2 Difference of the electrostatic potential ΔV (eV) between pore and wire obtained by DFT and RESP charges at different heights above the wire.

	nm		nm-H	
Height [Å]	ΔV_{DFT}	ΔV_{RESP}	ΔV_{DFT}	ΔV_{RESP}
2.8	0.640	0.615	0.156	0.157
3.8	0.535	0.511	0.108	0.119
4.8	0.438	0.411	0.088	0.094

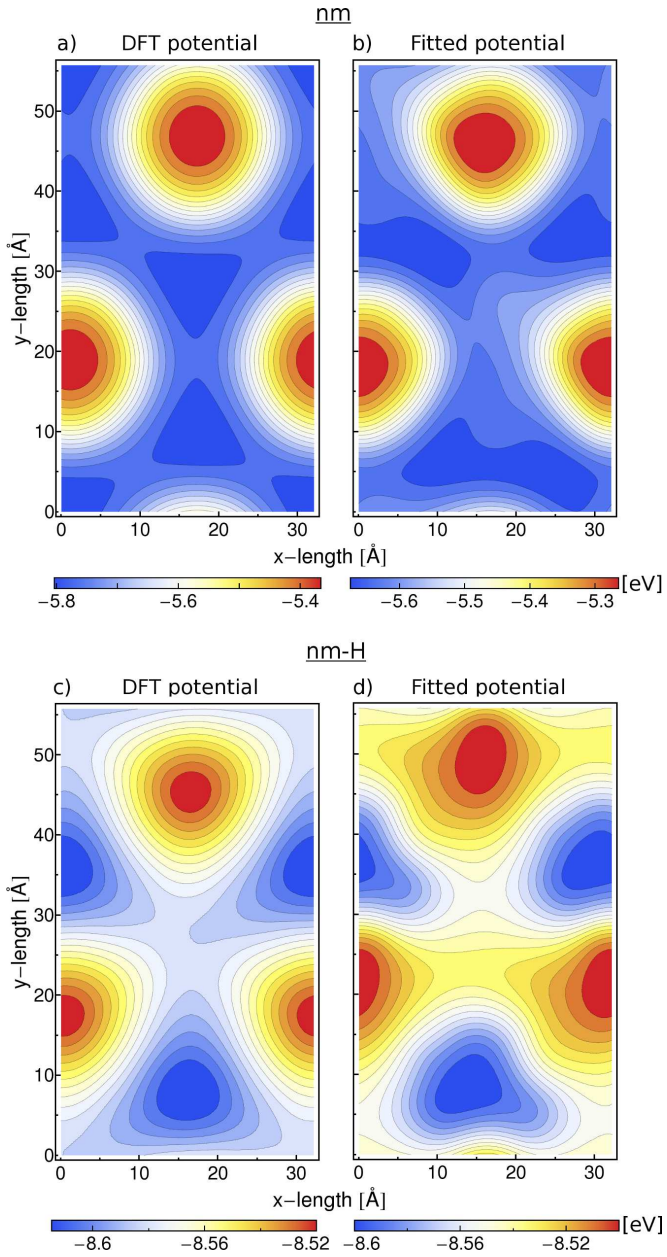

Fig. 4 Electrostatic potential at 4.8 Å above the wire. Potential for nm obtained by (a) DFT and (b) generated by RESP charges . (c) DFT potential and (d) fitted potential for nm-H.

modulation of the potential is observed, where the absolute values are smaller above the pore than above the wire. The fitted potential reproduces main features of V_{QM} qualitatively very well. The resemblance seems slightly worse for nm-H. Since nm-H is almost flat, the assignment of atoms to the pore and wire is somewhat delicate and influences highly the modulation of the fitted potential. Quantitatively, the potential difference ΔV between pore and wire is of primary importance and is reported in Table 2 for different heights above the wire. ΔV is generally well reproduced by the RESP charges for both systems and 4-5 times larger for nm. At 2.8 Å above the surface, the deviation compared to DFT is less than 4% for nm and 1% for nm-H. Further away from the surface - at 4.8 Å -, the deviation is a bit larger, but still less that 7%. Recalling that the potential was solely fitted between 2 to 4 Å above the slab, it is encouraging that even for regions outside the fitting range the potential is well represented by the RESP charges.

4.3 Structural and dynamic properties of water at the nm and nm-H interface

The structural properties and the dynamics of the liquid water film interacting with the two different substrates are investigated from the analysis of the MD trajectories. A typical snapshot of the water film on each substrate is presented in Figure 5(a and b). Radial distribution functions (RDFs) for different layers of the slab are reported in Figure S3 (SI) and are essentially identical for both systems. In the middle of the slab, the RDF reproduces the typical shape found for bulk liquid water.[60,61] The reduced peak heights obtained for RDFs of the interface regions are due to the diminished coordination. The slight difference in peak heights for the latter suggest that water is more structured at the substrate than at the vacuum.

The plane-averaged density of the water molecules ρ_w as function of the vertical distance from the surface is presented in Figure 5(c and d). Since the absolute height of BN changes depending on the corrugation and on the presence of intercalated H, the plane of the highest BN pairs was taken as reference ($z = 0$) to define the distance of the water molecules from the surface. Both systems show a sharp large peak at 3.1 Å (nm) and 3.2 Å (nm-H) where the density is more than twice as large as in bulk water. The adlayer is followed by a 2.0 Å broad region of density depletion with a significantly smaller density of 0.5 g/cm^3. A second broad peak is found at 6.0 Å showing that the water configuration is still dictated by the substrate. The first and second peak indicate that the water molecules at the interface are overstructured compared to bulk water. At larger distances, the density distribution is uniform corresponding to bulk water. The density decreases finally to zero at the liquid-vacuum interface. In the case of nm, an earlier onset of the density profile and an additional broad shoulder at 2.3 Å are observed. The 2D plot of the spatial distributions of O atoms at a distance of 2.3 Å, see Figure 5 (f), shows that water molecules are localized in the pore at this height, while none are found over the wire. This proofs that the water film follows the corrugation of the BN layer and confirms the visual impression obtained from the snapshot in Figure 5(a).

For further analysis, the water films are partitioned into four layers following the oscillations in the averaged density profile as shown in Figure 5(c and d). First information on the hydrogen bonding patterns at the interface are provided by the plane-averaged distributions of O and H atoms presented in Figure 5(e). The largest fraction of the hydrogens in the first

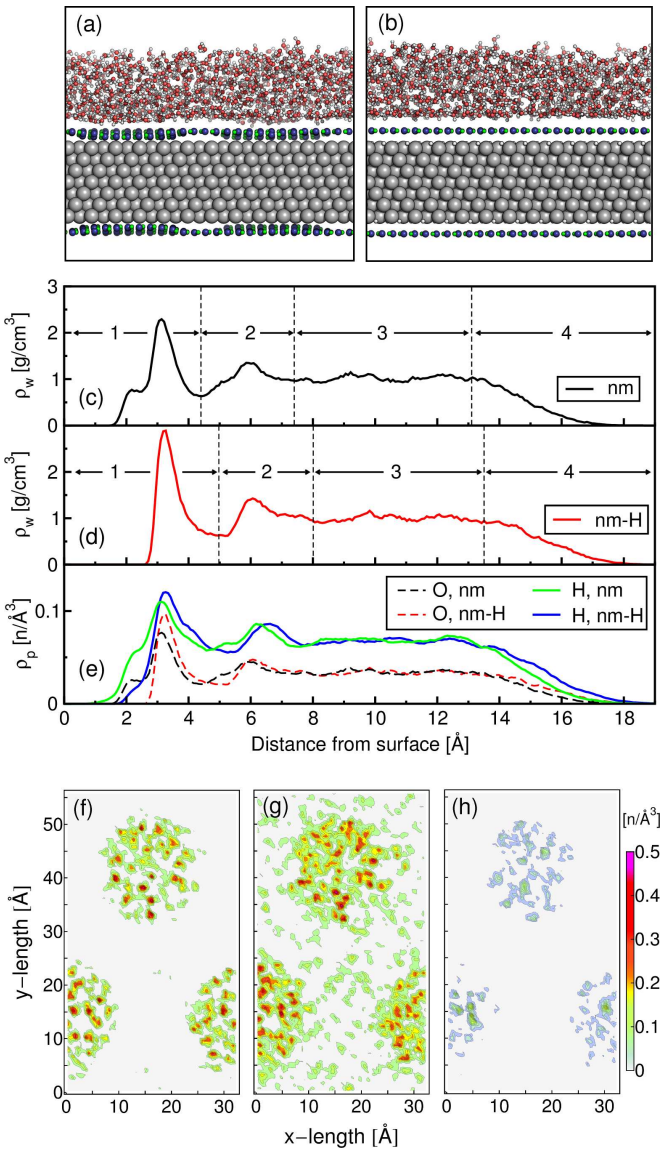

Fig. 5 Typical snapshot of the simulation cells of (a) water/nm and (b) water/nm-H. (c-e) Properties as function of the distance from the BN wire. Plane-averaged water density ρ_w along the surface normal (z-direction) for (c) water/nm and (d) water/nm-H. The arrows indicate the division of the water film in four different layers. (e) Plane-averaged particle densities ρ_p for O and H atoms. Spatial distribution of (f) O and (g) H atoms for water/nm at 2.3 Å from the wire. (h) Spatial distribution of H atoms at a distance of 1.2 Å.

layer is located in the plane of the O atoms indicated by the large peaks at 3.1 Å (nm) and 3.2 Å (nm-H). At this height, the H atom density is only 1.3 times larger compared to the O atom density, whereas a factor of two is expected for bulk water. This suggests that many H-bonds are formed with the acceptors of the second layer or the substrate. The H-bonds donated to the second layer are counted applying a standard criterion for defining a H-bond.[62,63] In both cases roughly 45% of the water molecules donate one H-bond to the second layer, but only 2% of them donate both. All the other H, which are not involved in a H-bond to a molecule in the second layer, form either an in-layer H-bond, or point toward the substrate. The onset of the H-distribution is for both systems at shorter distances than for oxygen alluding that H atoms point towards the surface. This is confirmed by the 2D plot of the spatial hydrogen distribution at 1.2 Å displayed in Figure 5(h) for water/nm. At distances smaller than 1.5 Å, the probability of finding O atoms is zero, whereas this not true for H atoms. Some water molecules located in the pore direct their hydrogens towards the substrate. This is also observed for molecules above the wire. At 2.3 Å, oxygen can be only found in the pore, but H atoms can be also found above the wire, see Figure 5(f and h).

The average number of accepted and donated H-bonds per molecule has been computed for further investigation of the hydrogen bonding properties. The distribution of H-bonds in each layer is plotted for water/nm in Figure 6(a). In the bulk-like part of the film, the second and third layer, most of the molecules are involved in four hydrogen bonds, which is in agreement with DFT-PBE studies of bulk water.[60,64–66] At the interface, the H-bonding is frustrated and the probability for forming three H-bonds is slightly larger than for a tetrahedral formation. Small differences between the H-bond distributions of the adlayer are observed comparing the two different substrates. As shown in panel (b) of Figure 6, the probability for three and four H-bonds are equivalent for the water/nm-H system indicating slightly less frustrated H-bond patterns imposed by the substrate.

Indication of a possible polarization of the molecules interacting with the substrate could be obtained by the analysis of the average orientation of the dipole moment. As first approximation to the dipole moment orientation, we consider angle α between surface normal and the vector **d** laying in the H_2O molecular plane and bisecting the HOH angle, as shown in Figure 7(a). An angle of 90° refers to a dipole orientation parallel to the surface. The vector **d** points away from the substrate if $0° \leq \alpha < 90°$ and towards the substrate if

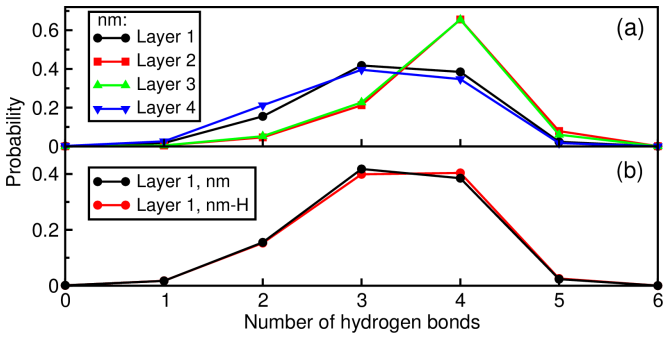

Fig. 6 Distribution of the total number of H-bonds per molecule. The layers of the water film are defined in Figure 5(a and b). (a) Distribution of H-bonds for water/nm. (b) Distribution of H-bonds at the water-substrate interface comparing water/nm and water/nm-H.

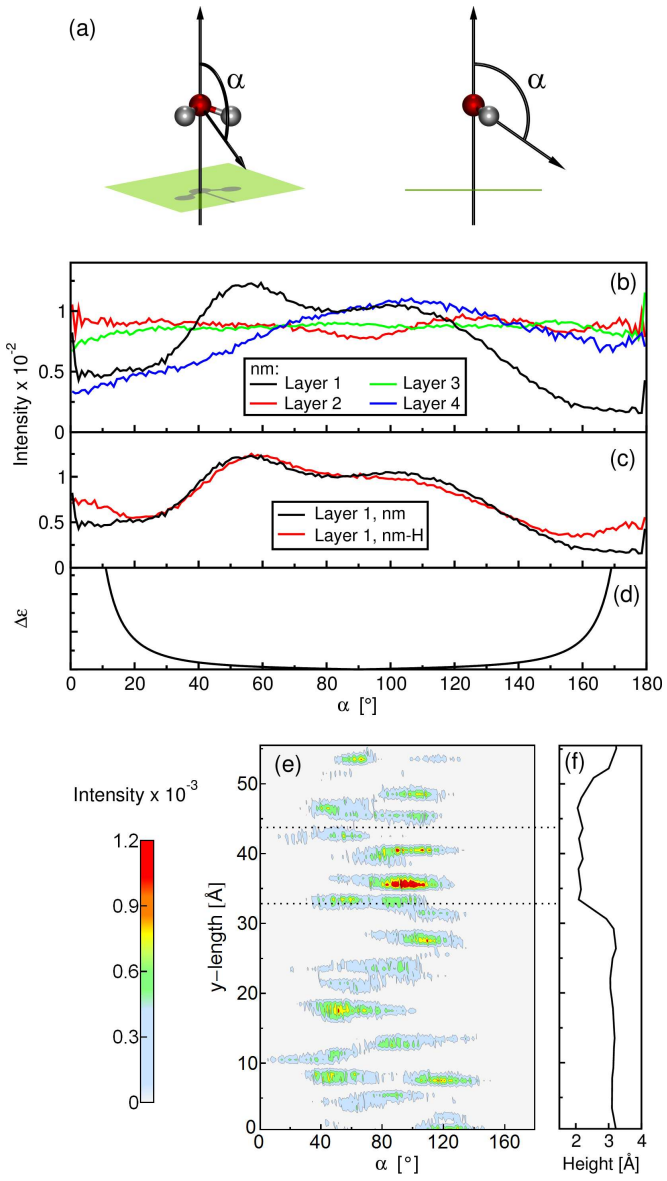

Fig. 7 Orientation of the dipole moment. (a) Definition of the orientation angle α with respect to the surface normal. (b) Distribution of α for each layer obtained for water/nm. (c) Distribution of α in the adlayer for water/nm and water/nm-H. (d) Absolute error $\Delta\varepsilon$ for the distribution of α. (e) Angle α correlated with the spatial distribution of water molecules along the horizontal y-dimensions of the orthorhombic unit cell of nm. (f) Height of the BN layer measured relative to the topmost Rh layer correlated with the y-dimension of the unit cell.

$90^\circ < \alpha \leq 180^\circ$. The distribution of α is shown for water/nm in Figure 7(b). Note that a homogeneous orientational distributions exhibits the shape of a sine with a maximum at 90°, which can be validated by simple trigonometric considerations. In this representation, it is difficult to evaluate if any angles are preferred. Therefore, the distributions have been normalized by $\sin\alpha$ such that for homogeneous distributions no or only a weak dependence on α is expected. Homogeneous distributions are found for layers two and three confirming their bulk-like nature, see Figure 7(b). At the liquid/vacuum interface, the distribution has a broad peak at around 105° indicating that the dipole moments are preferentially directed toward the bulk. The same is observed for the liquid/vacuum interfaces of a pure water slab, see Figure S4 (SI). This is understood with the tendency of water to optimize the number of H-bonds with other water molecules. Two peaks are instead observed for molecules belonging to the adlayer: one at 55° indicating an increased probability for the orientation towards the bulk and a second one at around $100^\circ - 110^\circ$, which corresponds to molecules turned towards the substrate. Molecule orientation towards the surface are associated with increased interactions between adlayer and substrate mediated by H-bonds.

Comparing the distributions in the first layer for water/nm and water/nm-H, we find that the orientation angle of $100^\circ - 110^\circ$ is less favored for water/nm-H, see Figure 7(c). This implies that the interactions with the surface are weaker for the flat nanomesh. The curves displayed in Figure 7(c) deviate also for $\alpha < 30^\circ$ and $\alpha > 150^\circ$. These differences must be attributed to technical artifacts. Due to limited sampling and the discrete nature of the distribution, each angle is error-prone. The errors are especially large for small and large angles, which is illustrated by $\Delta\varepsilon$ depicted in Figure 7(d). The functional form of the absolute error $\Delta\varepsilon(\alpha)$ is given by $\left|\frac{\partial(\sin\alpha)^{-1}}{\partial\alpha}\right|$.

We also want to determine whether the molecules orientated towards the substrate are preferentially located at specific sites of the nanomesh, i.e. pore or wire. For that reason, α is correlated with the spatial distribution of water molecules along the y-dimension of the unit cell at a fixed x-value, see Figure 7(e). In Figure 7(f), the corresponding *h*-BN height along the same line is reported, thus identifying the pore area between $30 - 50$ Å. We find that angle of $95^\circ - 110^\circ$ are more probable for water molecules in the pore pointing to stronger interaction here. This agrees well with previous DFT based studies where stronger interactions between water molecules and nanomesh are predicted for molecules trapped in the pore.[27]

In order to estimate the diffusivity of the water molecules on nm, the mean square displacement[67] (MSD) has been computed and is presented in Figure 8. The MSD has been measured for two sets of 23 water molecules belonging to the first layer over the pore and over the wire, respectively. The slope of the time-dependent MSD plot for molecules on the wire is clearly larger than for molecules in the pore. This indicates that the diffusivity within the pore is substantially reduced confirming that the modulated ESP tends to trap molecules there. These results agree with experimental and theoretical studies of nano-ice clusters on nm.[25,29] Based on scanning tunneling microscopy, Ma *et al.*[25] proposed the formation of stable ice hexamers in the pore, whereas well-defined structures have not been found on the wire. The latter has been

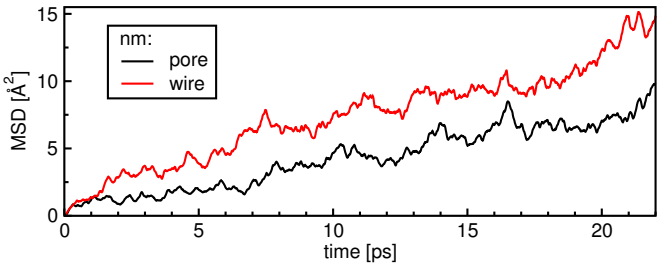

Fig. 8 MSD for water/nm observed for a set of 23 molecules located in the pore and in the wire, respectively.

Table 3 Interaction energy E_{int} (kJ/(mol·nm^2)) and ratio of solid-liquid γ_{SL} with respect to liquid-vacuum energy γ_{LV}.

	E_{int}	$-\frac{\gamma_{SL}}{\gamma_{LV}}$
water/nm	−90.9	1.026
water/nm-H	−87.4	0.987
Δ	−3.5	0.04

interpreted as result of the high mobility of weakly adsorbed molecules.

4.4 Wetting behavior

To assess the wetting behavior of water on nm and nm-H, interaction energies E_{int} and properties related to the contact angle θ have been computed, see Table 3. The interaction energy is 4% larger for water/nm indicating that the surface is more hydrophilic. Macroscopically, smaller contact angles correlate with a larger hydrophilicity of the surface. The contact angle θ is not directly accessible, but it can be related to the ratio $-\gamma_{SL}/\gamma_{LV}$ defined in Section 3.2. A larger ratio corresponds to a larger $\cos\theta$ and a smaller θ, given that $0° \leq \theta \leq 180°$. From our evaluation of the liquid/substrate interaction energies, we obtain that the ratio $-\gamma_{SL}/\gamma_{LV}$ is larger for water/nm predicting consequently a smaller contact angle. Taking the differences of both ratios, the resulting $\Delta\cos\theta$ is 0.04, which is a property that could potentially be confirmed by experimental studies.

The comparison to experiment is not straightforward due to the approximations implied in our model. First, the Young equation is an approximation assuming a static contact angle for a droplet on a surface, whereas in practice a range of angles is observed.[57] Also it is assumed that γ_{LV} is the same for the two systems, which is an approximation as well. Second, our theoretical model for describing the water/substrate interface is limited since the interactions between liquid and surface are treated at the MM level of theory. The electrostatic interactions are modeled accurately as demonstrated in Section 4.2. However, the dispersion interactions might be slightly overestimated which has been discussed in Section 4.1.

5 Conclusions

We introduced a method to fit RESP charges for periodic systems based on the GPW scheme and we applied it to study the wetting behavior of water on the *h*-BN/Rh nanomesh depending on the modulation of the ESP. The proposed periodic RESP method offers great flexibility in assigning the real space volumes where the reference ESP should be reproduced with higher accuracy. This allows to tune the calculation of RESP charges easily for nano-structured materials exposing surfaces and porous structures.

RESP charges have been determined to reproduce the ESP of two different substrates based on the *h*-BN/Rh interface, i.e. nm and nm-H. The first is characterized by a relative strong modulation of the potential, following the corrugation of the *h*-BN layer, while the effect for the second is reduced due to the presence of intercalated H atoms. The resulting charges have been used to model the interaction of the two substrates with liquid water within a QM/MM approach, where water is treated at the DFT level and the interaction to the substrate at the MM level.

Structural and dynamical properties of the two interfaces have been extracted from the analysis of the generated MD trajectories. We observe that the water film follows the corrugation of the *h*-BN layer for nm. In both cases the interaction of water with the substrate is responsible for the formation of an overstructured adlayer with an unfavorable H-bond network with respect to water's preferred tetrahedral structure. The effect of the frustration of the H-bonding appears to be slightly more pronounced at the nm than on the nm-H interface. By inspecting the average orientation of water molecules, an increased probability is found for molecules turned towards the substrate, which is in particular associated to molecules placed over the pore of nm. In addition to that, molecules close to the pore show a reduced diffusivity with respect to molecules staying over the wire.

Finally, interaction energies between substrate and water film and the surface energy of a free standing liquid water film are calculated. These energies are used to compare the wetting of water on nm and nm-H. We find that the nm surface is slightly more hydrophilic, as also shown by the structural investigation. Macroscopically, we predict a smaller contact angle for a droplet of water on nm than on nm-H.

6 Acknowledgments

We would like to thank Prof. Thomas Greber from the physics department at the University of Zurich for inspiring discussions, and the Swiss National Supercomputing Center (CSCS) for providing computational resources.

References

1 M. A. Henderson, *Surf. Sci. Rep.*, 2002, **46**, 1–308.

2 P. A. Thiel and T. E. Madey, *Surf. Sci. Rep.*, 1987, **7**, 211 – 385.
3 M. Corso, W. Auwärter, M. Muntwiler, A. Tamai, T. Greber and J. Osterwalder, *Science*, 2004, **303**, 217–220.
4 R. Laskowski, P. Blaha and K. Schwarz, *Phys. Rev. B*, 2008, **78**, 045409.
5 J. Gómez Díaz, Y. Ding, R. Koitz, A. P. Seitsonen, M. Iannuzzi and J. Hutter, *Theor. Chem. Acc.*, 2013, **132**, 1350.
6 S. Berner, M. Corso, R. Widmer, O. Groening, R. Laskowski, P. Blaha, K. Schwarz, A. Goriachko, H. Over, S. Gsell, M. Schreck, H. Sachdev, T. Greber and J. Osterwalder, *Angew. Chem. Int. Ed.*, 2007, **46**, 5115–5119.
7 A. B. Preobrajenski, A. S. Vinogradov and N. Mårtensson, *Surf. Sci.*, 2005, **582**, 21 – 30.
8 A. B. Preobrajenski, S. A. Krasnikov, A. S. Vinogradov, M. L. Ng, T. Käämbre, A. A. Cafolla and N. Mårtensson, *Phys. Rev. B*, 2008, **77**, 085421.
9 I. Shimoyama, Y. Baba, T. Sekiguchi and K. G. Nath, *J. Electron Spectrosc. Relat. Phenom.*, 2009, **175**, 6 – 13.
10 S. Joshi, D. Ecija, R. Koitz, M. Iannuzzi, A. P. Seitsonen, J. Hutter, H. Sachdev, S. Vijayaraghavan, F. Bischoff, K. Seufert, J. V. Barth and W. Auwärter, *Nano Lett.*, 2012, **12**, 5821–5828.
11 F. Orlando, R. Larciprete, P. Lacovig, I. Boscarato, A. Baraldi and S. Lizzit, *J. Phys. Chem. C*, 2012, **116**, 157–164.
12 F. Schulz, R. Drost, S. K. Hämäläinen and P. Liljeroth, *ACS Nano*, 2013, **7**, 11121–11128.
13 A. B. Preobrajenski, A. S. Vinogradov, M. L. Ng, E. Ćavar, R. Westerström, A. Mikkelsen, E. Lundgren and N. Mårtensson, *Phys. Rev. B*, 2007, **75**, 245412.
14 M. Morscher, M. Corso, T. Greber and J. Osterwalder, *Surf. Sci.*, 2006, **600**, 3280 – 3284.
15 F. Müller, S. Hüfner, H. Sachdev, R. Laskowski, P. Blaha and K. Schwarz, *Phys. Rev. B*, 2010, **82**, 113406.
16 T. Brugger, S. Günther, B. Wang, J. H. Dil, M.-L. Bocquet, J. Osterwalder, J. Wintterlin and T. Greber, *Phys. Rev. B*, 2009, **79**, 045407.
17 A. Goriachko, Y. He, M. Knapp, H. Over, M. Corso, T. Brugger, S. Berner, J. Osterwalder and T. Greber, *Langmuir*, 2007, **23**, 2928–2931.
18 R. Laskowski, P. Blaha, T. Gallauner and K. Schwarz, *Phys. Rev. Lett.*, 2007, **98**, 106802.
19 R. Laskowski and P. Blaha, *J. Phys.: Condens. Matter*, 2008, **20**, 064207.
20 H. Dil, J. Lobo-Checa, R. Laskowski, P. Blaha, S. Berner, J. Osterwalder and T. Greber, *Science*, 2008, **319**, 1824–1826.
21 M. Iannuzzi, F. Tran, R. Widmer, T. Dienel, K. Radican, Y. Ding, J. Hutter and O. Gröning, *Phys. Chem. Chem. Phys.*, 2014, **16**, 12374–12384.
22 S. Joshi, F. Bischoff, R. Koitz, D. Ecija, K. Seufert, A. P. Seitsonen, J. Hutter, K. Diller, J. I. Urgel, H. Sachdev, J. V. Barth and W. Auwärter, *ACS Nano*, 2014, **8**, 430–442.
23 P. Bacle, A. P. Seitsonen, M. Iannuzzi and J. Hutter, *CHIMIA*, 2014, **68**, 596–601.
24 R. Widmer, D. Passerone, T. Mattle, H. Sachdev and O. Gröning, *Nanoscale*, 2010, **2**, 502–508.
25 H. Ma, T. Brugger, S. Berner, Y. Ding, M. Iannuzzi, J. Hutter, J. Osterwalder and T. Greber, *ChemPhysChem*, 2010, **11**, 399–403.
26 H. Ma, Y. Ding, M. Iannuzzi, T. Brugger, S. Berner, J. Hutter, J. Osterwalder and T. Greber, *Langmuir*, 2012, **28**, 15246–15250.
27 Y. Ding, M. Iannuzzi and J. Hutter, *J. Phys. Chem. C*, 2011, **115**, 13685–13692.
28 Y. Ding, M. Iannuzzi and J. Hutter, *CHIMIA*, 2011, **65**, 256–259.
29 Y. Ding, M. Iannuzzi and J. Hutter, *J. Phys.: Condens. Matter*, 2012, **24**, 445002.
30 O. Bunk, M. Corso, D. Martoccia, R. Herger, P. R. Willmott, B. D. Patterson, J. Osterwalder, J. F. van der Veen and T. Greber, *Surf. Sci.*, 2007, **601**, L7 – L10.
31 R. Widmer, S. Berner, O. Gröning, T. Brugger, J. Osterwalder and T. Greber, *Electrochem. Commun.*, 2007, **9**, 2484–2488.
32 T. Brugger, H. Ma, M. Iannuzzi, S. Berner, A. Winkler, J. Hutter, J. Osterwalder and T. Greber, *Angew. Chem. Int. Ed.*, 2010, **49**, 6120–6124.
33 A. Warshel and M. Levitt, *J. Mol. Biol.*, 1976, **103**, 227–249.
34 D. Golze, M. Iannuzzi, M.-T. Nguyen, D. Passerone and J. Hutter, *J. Chem. Theory Comput.*, 2013, **9**, 5086–5097.
35 C. I. Bayly, P. Cieplak, W. D. Cornell and P. A. Kollman, *J. Phys. Chem.*, 1993, **97**, 10269–10280.
36 C. Campañá, B. Mussard and T. K. Woo, *J. Chem. Theory Comput.*, 2009, **5**, 2866–2878.
37 D.-L. Chen, A. C. Stern, B. Space and J. K. Johnson, *J. Phys. Chem. A*, 2010, **114**, 10225–10233.
38 *The CP2K developers group, CP2K is freely available from: http://www.cp2k.org/ (accessed May, 2014).*
39 J. Hutter, M. Iannuzzi, F. Schiffmann and J. VandeVondele, *WIREs Comput. Mol. Sci*, 2014, **4**, 15–25.
40 G. Lippert, J. Hutter and M. Parrinello, *Mol. Phys.*, 1997, **92**, 477–487.
41 J. VandeVondele, M. Krack, F. Mohamed, M. Parrinello, T. Chassaing and J. Hutter, *Comput. Phys. Commun.*, 2005, **167**, 103–128.
42 J. VandeVondele and J. Hutter, *J. Chem. Phys.*, 2007, **127**, 114105.
43 S. Goedecker, M. Teter and J. Hutter, *Phys. Rev. B*, 1996, **54**, 1703–1710.
44 C. Hartwigsen, S. Goedecker and J. Hutter, *Phys. Rev. B*, 1998, **58**, 3641–3662.
45 M. Krack, *Theor. Chem. Acc.*, 2005, **114**, 145–152.
46 Y. Zhang and W. Yang, *Phys. Rev. Lett.*, 1998, **80**, 890.
47 S. Grimme, J. Antony, S. Ehrlich and H. Krieg, *J. Chem. Phys.*, 2010, **132**, 154104.
48 P. Bendt and A. Zunger, *Phys. Rev. B*, 1982, **26**, 3114–3137.
49 J. P. Perdew, K. Burke and M. Ernzerhof, *Phys. Rev. Lett.*, 1996, **77**, 3865–3868.
50 T. Laino, F. Mohamed, A. Laio and M. Parrinello, *J. Chem. Theory Comput.*, 2005, **1**, 1176–1184.
51 T. Laino, F. Mohamed, A. Laio and M. Parrinello, *J. Chem. Theory Comput.*, 2006, **2**, 1370–1378.
52 J. W. Kang and H. J. Hwang, *J. Phys.: Condens. Matter*, 2004, **16**, 3901–3908.
53 C. Y. Won and N. R. Aluru, *J. Am. Chem. Soc.*, 2007, **129**, 2748–2749.
54 Y. Wu, H. L. Tepper and G. A. Voth, *J. Chem. Phys.*, 2006, **124**, 024503.
55 T. Young, *Philos. Trans. R. Soc. Lond.*, 1805, **95**, 65–87.
56 P. G. de Gennes, *Rev. Mod. Phys.*, 1985, **57**, 827–863.
57 Y. Yuan and T. R. Lee, in *Surface Science Techniques*, ed. G. Bracco and B. Holst, Springer, 2013, ch. Contact Angle and Wetting Properties, pp. 3–34.
58 B. Lange, R. Posner, K. Pohl, C. Thierfelder, G. Grundmeier, S. Blankenburg and W. Schmidt, *Surf. Sci.*, 2009, **603**, 60–64.
59 P. E. Blöchl, *J. Chem. Phys.*, 1995, **103**, 7422–7428.
60 L.-M. Liu, M. Krack and A. Michaelides, *J. Chem. Phys.*, 2009, **130**, 234702.
61 I.-C. Lin, A. P. Seitsonen, I. Tavernelli and U. Rothlisberger, *J. Chem. Theory Comput.*, 2012, **8**, 3902–3910.
62 A. Luzar and D. Chandler, *Phys. Rev. Lett.*, 1996, **76**, 928–931.
63 A. Luzar and D. Chandler, *Nature*, 1996, **379**, 55–57.
64 T. Todorova, A. P. Seitsonen, J. Hutter, I.-F. W. Kuo and C. J. Mundy, *J. Phys. Chem. B*, 2006, **110**, 3685–3691.
65 M. V. Fernández-Serra and E. Artacho, *J. Chem. Phys.*, 2004, **121**, 11136–11144.
66 D. Prendergast and G. Galli, *Phys. Rev. Lett.*, 2006, **96**, 215502.
67 M. P. Allen and D. J. Tildesley, *Computer Simulation of Liquids*, Oxford University Press, New York, 1992, pp. 204–208.